



# Force and torque reactions on a pitching flexible aerofoil

E. Sanmiguel-Rojas<sup>1</sup>, J.L. Perona<sup>1</sup> and R. Fernandez-Feria<sup>1,†</sup>

<sup>1</sup>Fluid Mechanics Group, University of Málaga, Dr Ortiz Ramos s/n, 29071 Málaga, Spain

(Received 4 July 2022; revised 14 February 2023; accepted 20 March 2023)

Experimental measurements in a wind tunnel of the unsteady force and moment that a fluid exerts on flexible flapping aerofoils are not trivial because the forces and moments caused by the aerofoil's inertia and others structural tensions at the pivot axis have to be obtained separately and subtracted from the direct measurements with a force/torque sensor. Here we derive from the nonlinear beam equation general relations for the force and torque reactions at the leading edge of a pitching aerofoil in terms of the fluid force and moment on the aerofoil and its kinematics, involving geometric and structural parameters of the flexible aerofoil. These relations are validated by comparing high-resolution numerical simulations of the flow–structure interaction of a two-dimensional flexible aerofoil pitching about its leading edge with direct force and torque measurements in a wind tunnel.

**Key words:** flow–structure interactions, swimming/flying, propulsion

## 1. Introduction

Relevant propulsion features of natural flyers and swimmers are captured by analysing basic motion modes of two-dimensional aerofoils such as pitching, heaving and their combinations (Lighthill 1969; Platzer *et al.* 2008; Wu 2011; Smits 2019; Wu *et al.* 2020). In particular, the study of flexibility effects on these simple flapping modes is of great importance because natural flyers and swimmers make use of flexible wings and fins to enhance their propulsion capabilities (Wu 1971; Katz & Weihs 1978; Pederzani & Haj-Hariri 2006; Heathcote & Gursul 2007; Zhu 2007; Alben 2008; Kang *et al.* 2011; Ramanarivo, Godoy-Diana & Thiria 2011; Dewey *et al.* 2013; Moore 2014; Fernandez-Feria & Alaminos-Quesada 2021; Peng *et al.* 2022).

† Email address for correspondence: [ramon.fernandez@uma.es](mailto:ramon.fernandez@uma.es)

Experimental measurements of the force and moment that the fluid exerts on the pitching and/or heaving flexible aerofoil are essential for these propulsive performance studies. They can be used directly to compute the thrust force and the propulsive efficiency of the aerofoil, or indirectly for the validation of numerical codes simulating the complex flow–structure interactions of the flapping flexible aerofoil. However, this is not a trivial task because what one measures with a force and torque sensor installed in a wind or a water tunnel are not the force and moment that the fluid exerts on the aerofoil, but the reactions on the axis where the aerofoil is attached to the sensor, so that the forces and moments caused by the aerofoil’s inertia and others structural tensions at the pivot axis have to be obtained separately. Different strategies have been used to solve this experimental difficulty. We focus here on the case of a flexible aerofoil undergoing pure pitching, including the rigid aerofoil as the limit of very large stiffness. For pure heave, the inertial torque is not needed to compute the power input as in the case of pitching (Heathcote & Gursul 2007).

Mackowski & Williamson (2015) considered a rigid aerofoil undergoing pure pitching, employing a force/torque sensor in a water channel, circumventing the above-mentioned difficulty by mounting an identical aerofoil and sensor out of the water flow and subtracting both measurements. Since air density is approximately a thousand times lower than water density, so are the force and moment that the air exerts on the aerofoil, and the measurement in air corresponds approximately to the inertial force and moment in comparison with the water measurement. Obviously, this technique cannot be used in wind tunnel experiments. It must also be emphasized that the aerofoil’s inertia effects on the force and moment measurements are approximately a thousand times more important in air than in water, greatly hindering direct measurements of the fluid force and moment on non-stationary aerofoils in a wind tunnel. In fact, inertial and aerodynamic forces are of the same order of magnitude in oscillating foils in air for reduced frequencies of interest in propulsion and energy harvesting applications (Siala, Kamrani Fard & Liburdy 2020). For a rigid aerofoil, the inertial contributions can be computed by just measuring synchronously with the force and torque the pitch angle  $\alpha(t)$ , but this is not enough for deformable aerofoils. To circumvent this difficulty for flexible aerofoils, several momentum-based and vortex-based approaches have been implemented experimentally for incompressible flows, but they involve high-resolution measurements of the flow field in a sufficiently large control volume around the aerofoil, and in most cases, these techniques provide just an estimation of the fluid force and moment (see e.g. the review by Rival & van Oudheusden 2017).

A novel technique is proposed here to compute the force and moment that the fluid exerts on a pitching flexible aerofoil in terms of the reaction force and torque at the pivot axis and the time evolution of a few points along the foil chord length. In the present paper, all these quantities are obtained by solving numerically the flow–structure interaction problem. The technique is validated by comparing the numerical results with experimental measurements in a wind tunnel of the reaction force and torque on a flexible aerofoil pitching about its leading edge. Although we use air as the fluid in numerical simulations and experiments, the technique is formulated in general for an incompressible flow, not limited to any density or viscosity of the fluid.

## 2. Formulation

We consider a two-dimensional flexible plate of chord length  $c$  and thickness  $\varepsilon$  immersed in a uniform fluid current of velocity  $U$  in the  $x$  direction and undergoing pitching motion

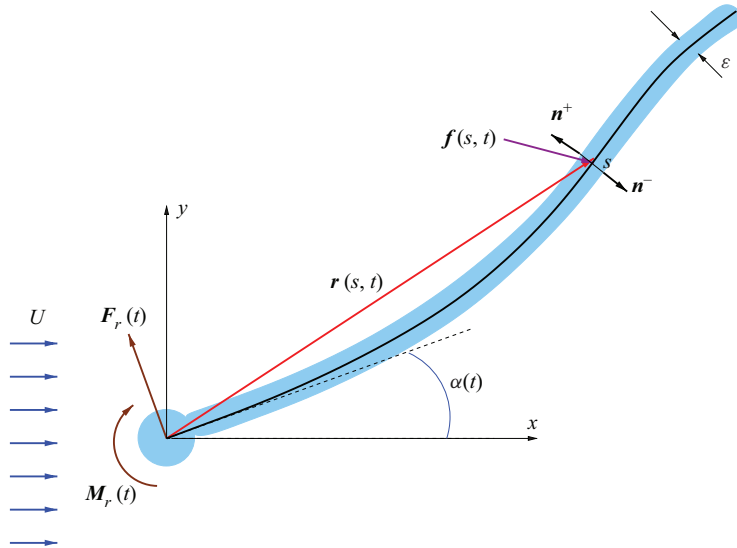


Figure 1. Schematic of the flexible pitching plate (dimensional quantities).

about the leading edge with angle

$$\alpha(t) = \alpha_0 \sin(2\pi ft) \tag{2.1}$$

in relation to the  $x$  axis (see [figure 1](#)), where  $\alpha_0$  and  $f$  are the pitch amplitude and frequency (in Hz), respectively. For a thin beam ( $\varepsilon/c \ll 1$ ) with structural bending rigidity  $EI$  and extensibility characterized by structural tension  $T$ , the nonlinear equation of motion can be written as ([Connell & Yue 2007](#))

$$\rho_s \varepsilon \frac{\partial^2 \mathbf{r}}{\partial t^2} - \frac{\partial}{\partial s} \left[ T(s, t) \frac{\partial \mathbf{r}}{\partial s} \right] + EI \frac{\partial^4 \mathbf{r}}{\partial s^4} = \mathbf{f}(s, t) + \mathbf{F}_r \delta(s - s_0) - \mathbf{g} \delta'(s - s_0), \tag{2.2}$$

$$T(s, t) = E\varepsilon \left[ 1 - \left( \frac{\partial \mathbf{r}}{\partial s} \frac{\partial \mathbf{r}}{\partial s} \right)^{-1/2} \right], \quad EI = \frac{E\varepsilon^3}{12}, \tag{2.3a,b}$$

with  $s$  the Lagrangian coordinate along the plate centreline,  $s = 0$  at the leading edge, and position vector  $\mathbf{r}(s, t)$  fixed at the leading edge. Here,  $\rho_s$  is the solid density and

$$\mathbf{f} = \boldsymbol{\tau}^+ \cdot \mathbf{n}^+ + \boldsymbol{\tau}^- \cdot \mathbf{n}^-, \quad \boldsymbol{\tau} = -p\mathbf{I} + \mu(\nabla \mathbf{u} + (\nabla \mathbf{u})^T), \tag{2.4a,b}$$

is the Lagrangian force (per unit area) exerted on the plate by the surrounding fluid, where  $\boldsymbol{\tau}$  is the fluid stress tensor,  $\mathbf{I}$  is the unit tensor, and  $\mathbf{n}^+$  and  $\mathbf{n}^-$  are the unit normal vectors on each side of the plate at the given point  $\mathbf{r}$  (see [figure 1](#)). The fluid pressure  $p$  and velocity  $\mathbf{u}$  satisfy the incompressible Navier–Stokes equations,

$$\nabla \cdot \mathbf{u} = 0, \quad \rho \left( \frac{\partial \mathbf{u}}{\partial t} + \mathbf{u} \cdot \nabla \mathbf{u} \right) = \nabla \cdot \boldsymbol{\tau}, \tag{2.5a,b}$$

with  $\rho$  and  $\mu$  being the fluid density and viscosity, respectively. The velocity boundary conditions are  $\mathbf{u} = \partial \mathbf{r} / \partial t$  on the fluid–plate moving boundary, and  $\mathbf{u} = U\mathbf{e}_x$  at infinity.

The last two terms on the right-hand side of (2.2) are included to account for the point reaction  $\mathbf{F}_r$  (per unit span) that fixes the leading edge at the origin of coordinates, and

for the point torque at the leading edge, modelled here as a couple of opposite point forces  $\pm \mathbf{g}$  that provide the necessary torque  $\mathbf{M}_r$  to generate the pitching motion (2.1). Mathematically, the localized force is modelled by Dirac's delta function  $\delta$ , and the torque by its derivative  $\delta'$  (Fernandez-Feria & Alaminos-Quesada 2021), both applied at point  $s = s_0$  that is chosen very close to the leading edge,  $s_0 \rightarrow 0^+$ , but not exactly at  $s = 0$  for structural (and mathematical) reasons.

The boundary conditions at the constrained leading edge are

$$\mathbf{r} = \mathbf{0} \quad \text{and} \quad \frac{\partial \mathbf{r}}{\partial s} = \cos \alpha(t) \mathbf{e}_x + \sin \alpha(t) \mathbf{e}_y \equiv \mathbf{e}_\alpha(t) \quad \text{at } s = 0, \quad (2.6)$$

where  $\mathbf{e}_\alpha(t)$  is the unit vector tangent to the aerofoil at the leading edge, while at the free trailing edge of the plate,

$$-T \frac{\partial \mathbf{r}}{\partial s} + EI \frac{\partial^3 \mathbf{r}}{\partial s^3} = \mathbf{0}, \quad \frac{\partial^2 \mathbf{r}}{\partial s^2} = \mathbf{0} \quad \text{at } s = s_f \simeq c, \quad (2.7)$$

where  $s_f(t)$  is the length of the plate at the instant  $t$ , which for large extensional rigidity is practically equal to  $c$ .

Integrating (2.2) between  $s = 0$  and  $s = s_f$ , using integration by parts and applying the above boundary conditions, one obtains the reaction  $\mathbf{F}_r$  at the leading edge (actually at  $s_0 \simeq 0$ ) as

$$\begin{aligned} \mathbf{F}_r(t) &= -\mathbf{F}(t) + \rho_s \varepsilon \int_0^{s_f} \frac{\partial^2 \mathbf{r}(s, t)}{\partial t^2} ds - T(0, t) \mathbf{e}_\alpha(t) + EI \left[ \frac{\partial^3 \mathbf{r}}{\partial s^3} \right]_{s=0}, \\ \mathbf{F}(t) &\equiv \int_0^{s_f} \mathbf{f}(s, t) ds, \end{aligned} \quad (2.8)$$

where  $\mathbf{F}$  is the total force (per unit span) exerted by the fluid on the plate. On the other hand, multiplying (2.2) vectorially by  $\mathbf{r}$  and integrating between  $s = 0$  and  $s = s_f$ , using again integration by parts and the boundary conditions, the torque at the leading edge can be written as

$$\mathbf{M}_r(t) \equiv \mathbf{e}_\alpha \wedge \mathbf{g}(t) = -\mathbf{M}(t) + \rho_s \varepsilon \int_0^{s_f} \mathbf{r} \wedge \frac{\partial^2 \mathbf{r}(s, t)}{\partial t^2} ds - EI \left[ \frac{\partial \mathbf{r}}{\partial s} \wedge \frac{\partial^2 \mathbf{r}}{\partial s^2} \right]_{s=0}, \quad (2.9)$$

where

$$\mathbf{M}(t) \equiv \int_0^{s_f} \mathbf{r} \wedge \mathbf{f}(s, t) ds \quad (2.10)$$

is the total bending moment (per unit span) with respect to the leading edge that the fluid exerts on the aerofoil.

The last terms in (2.8) and (2.9) evaluated at  $s = 0$  come from the fact that the leading edge is not a free end like the trailing edge, but it is constrained with the pitching motion (2.6). If the stretching stiffness is very large – more precisely, if the non-dimensional stretching stiffness is  $K = E\varepsilon/(\rho U^2 c) \gg 1$  – in first approximation  $|\partial \mathbf{r}/\partial s| = 1$ ,  $T = 0$ ,  $s_f = c$ , and one can neglect the second term in (2.2). Consequently, the term in (2.8) containing the tension  $T$  at the leading edge can be neglected. On the other hand, according to the condition (2.6), the position vector close to the leading edge (i.e. for small  $s$ ) can be

written as

$$\mathbf{r}(s, t) = s \mathbf{e}_\alpha(t) + \left[ \frac{\partial^2 \mathbf{r}}{\partial s^2} \right]_{s=0} \frac{s^2}{2} + \left[ \frac{\partial^3 \mathbf{r}}{\partial s^3} \right]_{s=0} \frac{s^3}{6} + \dots, \quad (2.11)$$

which allows the computation of the derivatives at  $s = 0$  of the last terms in (2.8) and (2.9) proportional to the bending rigidity  $EI$  from the knowledge of  $\mathbf{r}$  near the leading edge, calculated either numerically or experimentally. Clearly, these terms vanish for a rigid foil, where  $\mathbf{r}(s, t) = s \mathbf{e}_\alpha(t)$  everywhere (see below). But even for flexible foils, in practical applications the bending rigidity has to be sufficiently large for efficient propulsion (e.g. Alben 2008; Moore 2014), and though the flexural deflection may become large in some parts of the foil, at the leading edge the curvature cannot be large if the actuating torque has to generate an efficient pitching motion of the foil. Thus these terms evaluated at the leading edge are usually small compared with the inertial terms in most practical applications (see § 3), and will be neglected in what follows.

Equations (2.8) and (2.9) provide the force and torque  $\mathbf{F}_r(t)$  and  $\mathbf{M}_r(t)$  that one has to apply at the leading edge to generate the desired pure pitching motion (2.1) in terms of the fluid force and moment,  $\mathbf{F}(t)$  and  $\mathbf{M}(t)$ , and the kinematics  $\mathbf{r}(s, t)$  of the flexible aerofoil of known structural parameters and geometry. Alternatively, these equations provide the fluid force and moment,  $\mathbf{F}(t)$  and  $\mathbf{M}(t)$ , if the reactions  $\mathbf{F}_r(t)$  and  $\mathbf{M}_r(t)$  are measured experimentally and the instantaneous position  $\mathbf{r}(s, t)$  of the flexible aerofoil is obtained either numerically or experimentally. Here,  $\mathbf{r}(s, t)$  is obtained numerically along with  $\mathbf{F}(t)$  and  $\mathbf{M}(t)$ , and the resulting  $\mathbf{F}_r(t)$  and  $\mathbf{M}_r(t)$  will be compared with experimental measurements in a wind tunnel. But the expressions can be used the other way around, to obtain  $\mathbf{F}(t)$  and  $\mathbf{M}(t)$  from experimental measurements of  $\mathbf{F}_r(t)$  and  $\mathbf{M}_r(t)$ , and simultaneous video recording of the aerofoil motion to determine  $\mathbf{r}(s, t)$ .

For a rigid aerofoil, i.e. when the non-dimensional stiffness ratio is  $S = E\varepsilon^3 / (\rho U^2 c^3) \gg 1$ , one has  $\mathbf{r}(s, t) = s \mathbf{e}_\alpha(t) = s[\cos \alpha(t) \mathbf{e}_x + \sin \alpha(t) \mathbf{e}_y]$ . Thus  $\mathbf{r}$  is known if  $\alpha(t)$  is known, and the inertial and structural terms in (2.8) and (2.9) can be obtained analytically (all the structural terms at  $s = 0$  vanish):

$$\mathbf{F} = -\mathbf{F}_r + \frac{mc}{2} [-(\dot{\alpha}^2 \cos \alpha + \ddot{\alpha} \sin \alpha) \mathbf{e}_x + (-\dot{\alpha}^2 \sin \alpha + \ddot{\alpha} \cos \alpha) \mathbf{e}_y], \quad (2.12)$$

$$\mathbf{M} = -\mathbf{M}_r + \frac{mc^2}{3} \ddot{\alpha} \mathbf{e}_z, \quad (2.13)$$

where  $m = \rho_s \varepsilon c$  is the mass of the aerofoil per unit span, and the dots denote time derivatives. These expressions can be used to determine  $\mathbf{F}(t)$  and  $\mathbf{M}(t)$  just measuring  $\alpha(t)$  synchronously with  $\mathbf{F}_r(t)$  and  $\mathbf{M}_r(t)$ .

For a flexible aerofoil, the inertial and structural terms on the right-hand sides of (2.12) and (2.13) are more complex and cannot be obtained analytically, in general. They have to be computed by integrating numerically the second terms on the right-hand sides of (2.8) and (2.9), and computing the derivatives of  $\mathbf{r}(s, t)$  at  $s = 0$  for the additional terms associated with the rigidities of the aerofoil at the leading edge, once the kinematics of the foil  $\mathbf{r}(s, t)$  is obtained experimentally or numerically. In either case, one may discretize the aerofoil initial centreline into  $N$  segments of length  $\Delta s = c/N$  to follow the time evolutions of the positions of each segment central point:  $\mathbf{r}_i(t) = x_i(t) \mathbf{e}_x + y_i(t) \mathbf{e}_y$ ,  $i = 1, \dots, N$ . Then the terms containing  $\mathbf{r}$  in (2.8) and (2.9) are approximated by finite differences. Using, for instance, first-order finite differences and neglecting, as mentioned before, the structural terms at  $s = 0$ , one obtains the following approximate relations between  $[\mathbf{F}_r(t)$ ,

$\mathbf{M}_r(t)$ ] and  $[\mathbf{F}(t), \mathbf{M}(t)]$ :

$$\mathbf{F} \simeq -\mathbf{F}_r + \sum_{i=1}^N m_i \ddot{\mathbf{r}}_i, \tag{2.14}$$

$$\mathbf{M} \simeq -\mathbf{M}_r + \sum_{i=1}^N m_i \mathbf{r}_i \wedge \ddot{\mathbf{r}}_i, \tag{2.15}$$

where  $m_i = \rho_s \varepsilon (\Delta s)$  is the mass (per unit span) of each element of the plate. For a rigid aerofoil,  $\mathbf{r}_i = (i - 1/2)(\Delta s)\mathbf{e}_\alpha$ , and one recovers exactly the analytical expressions (2.12) and (2.13), knowing that  $m = \sum_{i=1}^N m_i = Nm_i$  and  $c = N(\Delta s)$ . The effect of flexibility on inertia force and moment can be obtained by substituting  $\mathbf{r}_i(t) = (i - 1/2)(\Delta s)\mathbf{e}_\alpha(t) + \mathbf{d}_i(t)$  into (2.14) and (2.15) and subtracting (2.12) and (2.13), respectively.

Although the approximations made in (2.14) and (2.15) have errors of the order of  $\Delta s = c/N$ , we will show in § 3 that  $N$  need not be very large to get an excellent approximation of the inertial terms if the bending stiffness is not too low.

### 3. Numerical method and results

The flow–structure interaction (FSI) problem is solved numerically using the coupled fluid and solid equations of motion discretized in both the fluid and plate domains separated by a moving boundary. In addition to (2.5a,b) for the fluid, more general differential structural equations inside the plate are used instead of the thickness-averaged nonlinear equation of motion (2.2), as described in Sanmiguel-Rojas & Fernandez-Feria (2021), but now for the pitching motion (2.1) imposed at the leading edge instead of a heaving motion. For both fluid and solid, the finite-volume-based solver Ansys Fluent is used, with the well known  $k-\omega$  SST turbulence model for the fluid, and the intrinsic FSI algorithm to simulate the fluid–structure coupling. For the Reynolds numbers considered (approximately  $10^5$ ; see § 4), the  $k-\omega$  SST turbulence model implemented in the solver package Ansys Fluent has been sufficiently validated experimentally for transitional flows in similar aerodynamic problems (e.g. Gharali & Johnson 2013). All simulations are started from rest. The harmonic motion (2.1) is emulated by a user-defined function. Actually, to avoid spurious initial oscillations,  $\alpha(t) = [(1 + \tanh((t - t_0)/t_1))/2]\alpha_0 \sin(2\pi ft)$  is used in place of (2.1), with  $t_0 = 0.1/f$  and  $t_1 = 0.5/f$ .

The computational domain, which reproduces the dimensions of the wind tunnel test section described in § 4, together with the different regions into which the computational domain is decomposed to ease the meshing procedure, is given in figure 2(a). Figure 2(b) shows the dimensions of the computational domain and the aerofoil (not to scale). With larger computational domains, the results practically did not change even in the most demanding cases. The aerofoil, of chord length  $c = 0.3$  m, consists of a steel plate with thickness  $\varepsilon = 0.4$  mm attached to an aluminium head of diameter 12 mm. These dimensions correspond to the aerofoil used in the experiments described in § 4. The boundary conditions are: a flat velocity profile at a length  $3.5c$  upstream of the foil; non-slip walls on the foil and tunnel walls; and an outlet boundary condition with pressure  $p = 0$  at a length  $10c$  downstream of the aerofoil. Air is used in all the computations ( $\rho = 1.225 \text{ kg m}^{-3}$ ,  $\mu = 1.789 \times 10^{-5} \text{ kg m}^{-1} \text{ s}^{-1}$ ). Details about the mesh and the grid convergence study are given in the Appendix.

## Force and torque reactions on a pitching flexible aerofoil

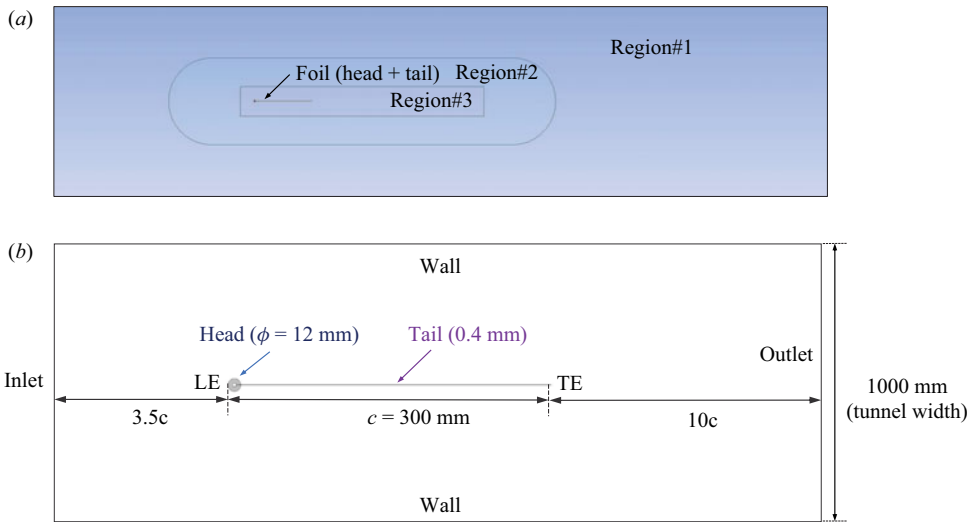


Figure 2. (a) Computational domain and mesh grid regions (to scale). (b) Dimensions used in the computations and the wind tunnel experiments, not to scale. LE, leading edge; TE, trailing edge.

Once the FSI problem is solved numerically for a given aerofoil and given values of  $U$ ,  $\alpha_0$  and  $f$ , the force  $F(t)$  and moment  $M(t)$  that the fluid exerts on the flexible aerofoil at each instant  $t$  are computed. In addition, the position  $r(s, t)$  of the foil centreline is also recorded at the same instants of time. With this information, one may compute the reactions at the leading edge  $F_r(t)$  and  $M_r(t)$  from (2.14) and (2.15) by discretizing the aerofoil centreline into  $N$  segments and using the time evolution of their central points  $r_i(t)$ .

Interestingly, it is found that even with a relatively small number of elements, the approximation made in (2.14) and (2.15) works quite well. This is shown in figure 3, where the two components of  $F_r(t)$  and the only component of  $M_r(t)$  are compared as the number  $N$  of plate elements used in the approximations (2.14) and (2.15) is increased, once  $F(t)$  and  $M(t)$  are computed numerically. In particular, the results obtained with  $N = 3, 6, 11$  and  $21$  plate elements are compared for one of the most unfavourable cases considered in the experimental measurements reported in § 4, with a flexural deflection at the trailing edge of approximately  $0.15c$  (see figure 4). The results are practically indistinguishable. (In figure 3,  $F(t)$  and  $M(t)$  are also shown, with dotted lines, for reference, showing that they are quite different from  $F_r(t)$  and  $M_r(t)$ .) This property makes this method very suitable for experimentation, for  $F(t)$  and  $M(t)$  may be computed from (2.14) and (2.15), measuring  $F_r(t)$  and  $M_r(t)$ , and simultaneously recording the position of just a few marker points  $r_i(t)$  along the flexible plate chord length. It is also checked that the contributions of the structural terms at  $s = 0$  in (2.8) and (2.9), neglected in (2.14) and (2.15), are very small, less than  $1.2 \times 10^{-3} \text{ N}$  and  $4.5 \times 10^{-4} \text{ N m}$ , respectively, in the case considered in figure 3.

The method can in principle be applied to any flexural deflection of the plate, with no maximum deflection limit (or minimum stiffness limit). Obviously, the reactions would not converge with just a few points if the bending rigidity is small. However, as mentioned above, the bending rigidity has to be large enough in practical applications for efficient propulsion. Just for reference sake, the non-dimensional bending stiffness  $EI/(\rho U^2 c^2)$  of the case considered in figure 3 is approximately unity, with a flexural deflection at the

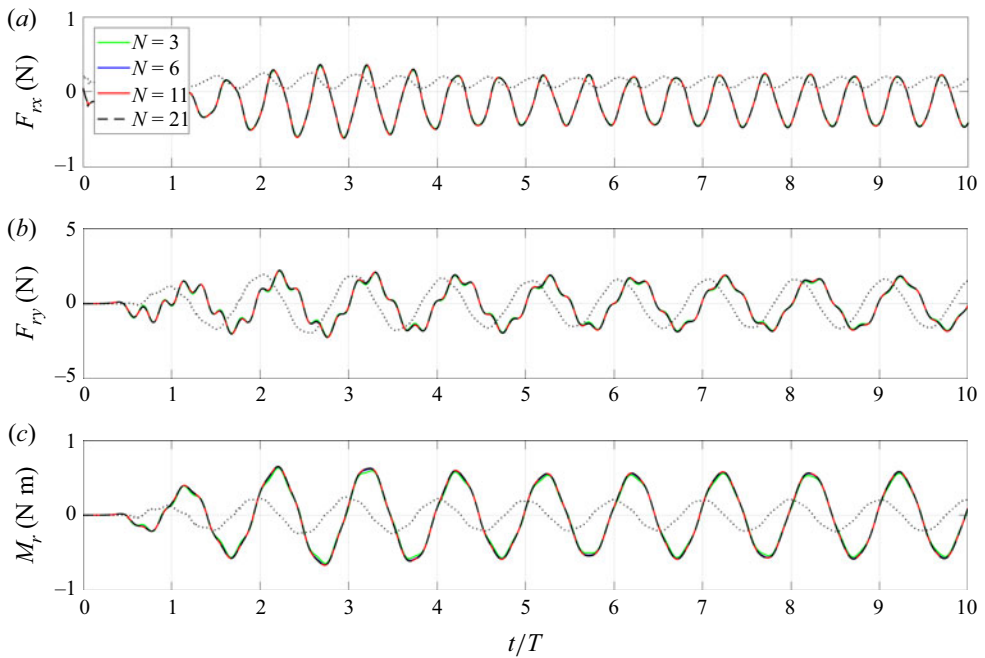


Figure 3. Comparison of  $F_r(t)$  and  $M_r(t)$  computed with different numbers  $N$  of plate elements for the inertial terms, as indicated, for a steel plate with  $c = 0.3$  m,  $\varepsilon = 0.4$  mm, span 0.31 m,  $U = 7$  m s<sup>-1</sup>,  $\alpha_0 = 3^\circ$  and  $f = 5$  Hz. Dotted lines correspond to  $F(t)$  and  $M(t)$ .

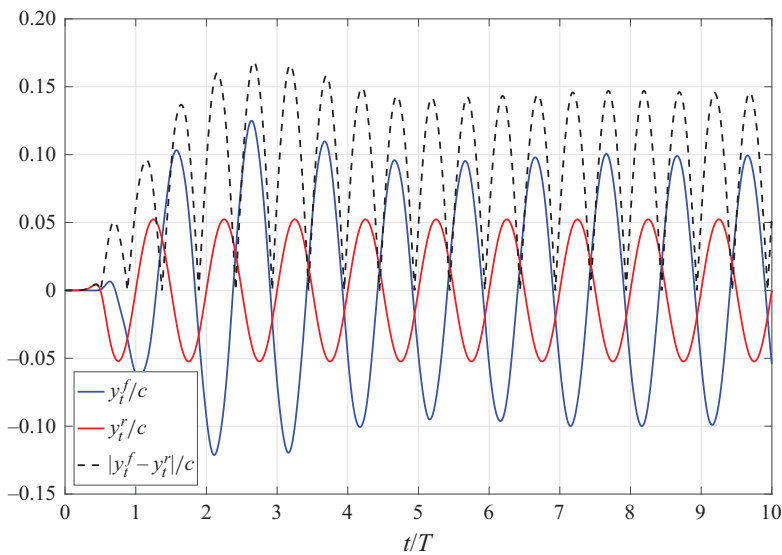


Figure 4. Flexural deflection at the trailing edge  $|y_t^f - y_t^r|/c$  (dashed line) for the same case plotted in [figure 3](#), where  $y_t^f$  is the trailing edge position of the flexible foil (blue line), and  $y_t^r$  is that of an otherwise identical rigid foil (red line).

## Force and torque reactions on a pitching aerofoil

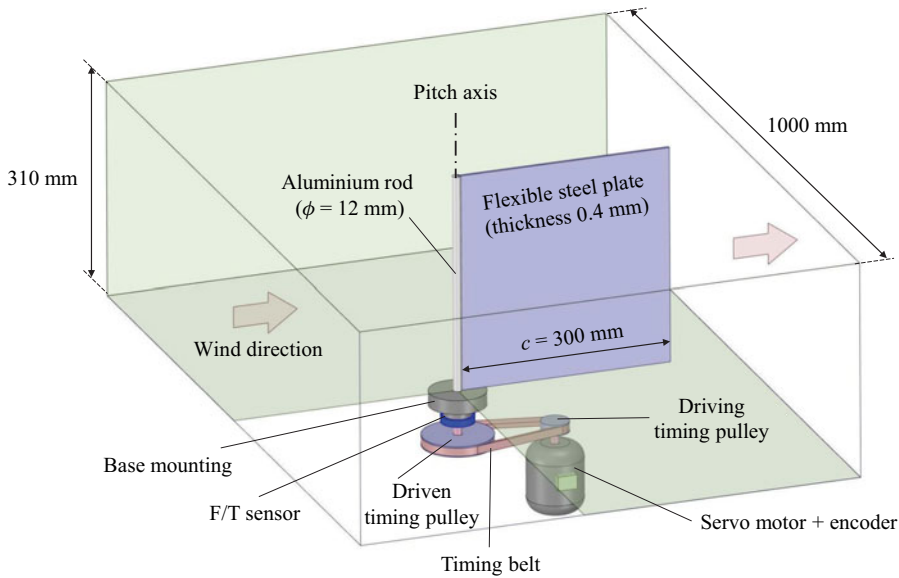


Figure 5. Experimental set-up in the wind tunnel test section.

trailing edge that is not too small, as shown in [figure 4](#). In spite of that, the reactions converge with only three points.

### 4. Validation with experimental measurements in a wind tunnel

As mentioned above, to validate this technique for computing  $F(t)$  and  $M(t)$  when  $F_r(t)$  and  $M_r(t)$  are measured, we proceed in an indirect way, without measuring  $r(s, t)$  simultaneously to  $F_r(t)$  and  $M_r(t)$ , but solving the problem numerically for  $F(t)$ ,  $M(t)$  and  $r(t)$ , and applying (2.14) and (2.15) to compute  $F_r(t)$  and  $M_r(t)$ , which then are compared with the reaction force and torque at the leading edge measured experimentally in a wind tunnel.

For the experiments, we use the subsonic, closed-circuit wind tunnel in the Aero-hydrodynamics Laboratory at the University of Malaga, with a test section of  $1 \times 1 \text{ m}^2$  cross-section that is 4 m long. An aerofoil of chord length  $c = 0.3 \text{ m}$ , consisting of a thin steel ( $\rho_s = 7864 \text{ kg m}^{-3}$ ,  $E = 2.1 \times 10^{11} \text{ Pa}$ ) plate of thickness  $\varepsilon = 0.4 \text{ mm}$ , with its leading edge embedded into an aluminium rod of diameter 12 mm, is mounted vertically onto the force/torque (F/T) sensor installed on the base of the wind tunnel test section 2 m from its inlet, with resolution 0.006 N and 0.001 N m. The steel plate span is 0.31 m, but an endplate on its top, with a gap of 5 mm, ensures the two-dimensionality of the flow along the major part of the aerofoil, and reduces end effects (see [figure 5](#); the effective test section is  $1 \times 0.31 \text{ m}^2$ ).

The inlet velocity  $U$ , measured with a hot wire anemometer (KIMO CTV210), ranges between 0 and  $7 \text{ m s}^{-1}$  in the present experimental runs, well below the maximum velocity provided by the wind tunnel of approximately  $40 \text{ m s}^{-1}$ . The free stream turbulence intensity is always less than 3%. The aerofoil is attached through the aluminium rod at its leading edge to a rotational servo motor, with position feedback provided by a high-resolution rotary encoder. The rotation is transmitted from the motor to the aluminium rod through two pulleys and a timing belt, with transmission relation 10 : 3.

Thus an accurate harmonic pitching motion  $\alpha(t)$  can be transmitted to the aerofoil's leading edge, with amplitude ranging between 2 and 6 degrees, and frequency between 3 and 6 Hz in the present experimental runs. The velocity  $U$  was varied between 0 and  $7 \text{ m s}^{-1}$ .

Experimental data of the three force and torque components – pitch angle, and free stream wind velocity and temperature – are synchronized and recorded in a computer through a data acquisition card controlled by the software LabVIEW, with sampling frequency 1000 Hz. Noise from mechanical vibrations and electronic devices is filtered with a seven-order low-pass Butterworth filter, with cut-off frequency  $2f + 2 \text{ Hz}$  for  $F_{rx}$ ,  $3f + 3$  for  $F_{ry}$ , and  $f + 2$  for  $M_r$ . Every experimental run, with a measurement duration of more than 15 s, is repeated at least three times, from which the standard deviation of each experimental measurement is also recorded.

The aerofoil and F/T sensor rotate together, and an alignment of the sensor coordinates with the free stream is necessary before each experimental run for given  $\alpha_0$  and  $U$ . This is made by measuring the forces on the static aerofoil at different angles between  $-\alpha_0$  and  $+\alpha_0$  to find the angle at which the modulus of the measured force,  $F_r = \sqrt{F_{rx}^2 + F_{ry}^2}$ , reaches a minimum. The corresponding angle is then summed to  $\alpha(t)$  in the projections of  $F_r$ .

Among the many experimental data recorded for different values of  $\alpha_0$ ,  $U$  and  $f$  in the ranges mentioned above, [figures 6](#) and [7](#) show two examples of the forces and torque measured experimentally through the F/T sensor,  $F_{rx}(t)$ ,  $F_{ry}(t)$  and  $M_r(t)$ , compared with the results of the numerical simulations under identical conditions of  $\alpha(t) = \alpha_0 \sin(2\pi ft)$  and  $U$ . Note that time is scaled in [figures 6](#) and [7](#) with the period  $T = 1/f$ . The corresponding Reynolds number and the reduced frequency, defined as  $Re = \rho c U / \mu$ ,  $k = \pi f c / U$ , respectively, are also included in the figure captions for reference. Both  $\rho$  and  $\mu$  are computed using the instantaneous temperature measurements of the air stream at the inlet of the wind tunnel test section. Also included in the figures are the force and moment exerted by the fluid on the aerofoil,  $F_x(t)$ ,  $F_y(t)$  and  $M(t)$ , as they are obtained numerically. Actually, numerically one obtains  $\mathbf{F}$  and  $\mathbf{M}$  by solving the FSI problem as described in § 3, and then computes  $F_r$  and  $M_r$  from (2.14) and (2.15). As mentioned above, the experimental values of  $F_{rx}(t)$ ,  $F_{ry}(t)$  and  $M_r(t)$ , plotted with black dashed lines in [figures 6](#) and [7](#), correspond to the mean values of at least three experimental runs, while the uncertainty bands are obtained from the standard deviations of these measurements. The uncertainty bands are noticeable only in [figure 6](#), being almost indistinguishable from the mean values for the case plotted in [figure 7](#).

Although the components of  $\mathbf{F}$  and  $\mathbf{M}$  are quite different from the components of  $F_r$  and  $M_r$  in the two cases shown in [figures 6](#) and [7](#) (and this is so for all the other experiments made), indicating that inertial forces are usually very important in wind tunnel force and torque measurements, the components of  $F_r$  and  $M_r$  obtained numerically practically coincide with those measured experimentally. The agreement remains as good as that shown in [figures 6](#) and [7](#) in most of the more than 40 cases investigated in the ranges of  $\alpha_0$ ,  $U$  and  $f$  mentioned above. [Figure 8](#) summarizes the comparison between reaction forces and moments measured experimentally and computed numerically for all the cases with  $U = 5 \text{ m s}^{-1}$ , which is by far the velocity most used in the wind tunnel experimental measurements. In particular, we plot the peak-to-peak oscillation amplitudes of the two reaction force components, denoted by  $\Delta F_{rx}$  and  $\Delta F_{ry}$  in [figures 8\(a\)](#) and [8\(b\)](#), and the reaction torque amplitude,  $\Delta M_r$  in [figure 8\(c\)](#), all of them obtained as an average from the last ten cycles in each case, measured or computed, for five different pitch amplitudes

Force and torque reactions on a pitching flexible aerofoil

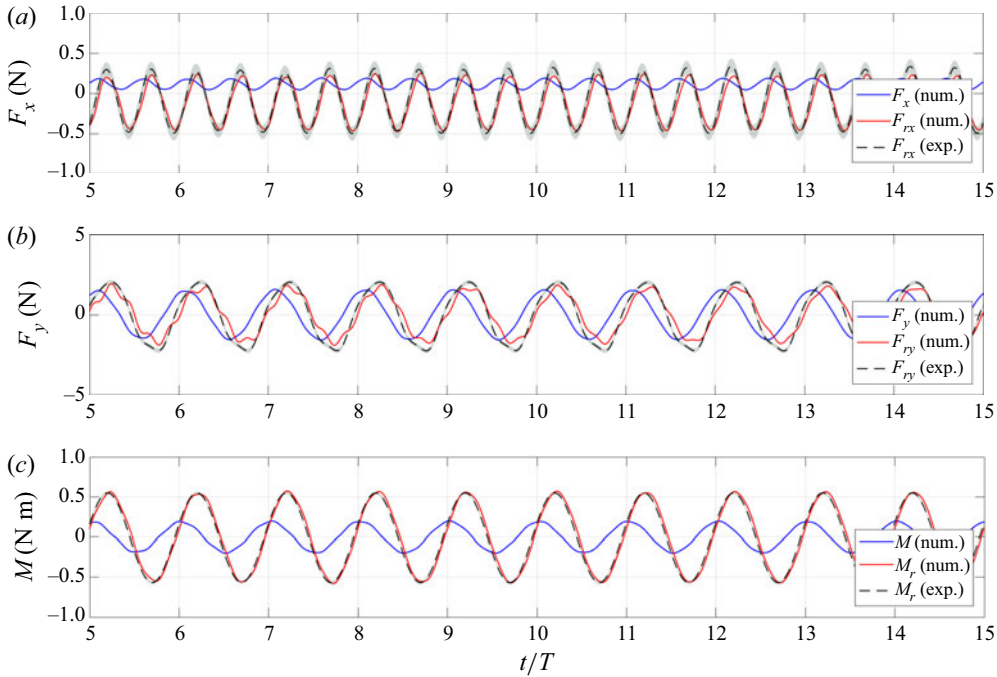


Figure 6. The two components of the reaction force  $F_r$  and the torque  $M_r$  measured experimentally (black dashed lines, with bands accounting for the experimental uncertainty) compared with numerical results obtained with mesh #1 and  $N = 21$  (red lines) for  $\alpha_0 = 3^\circ$ ,  $U = 7 \text{ m s}^{-1}$  and  $f = 5 \text{ Hz}$  ( $Re = 1.37 \times 10^5$  and  $k = 0.675$ ). Also shown with continuous blue lines are the components of the force  $F$  and the moment  $M$  that the fluid exerts on the plate obtained numerically.

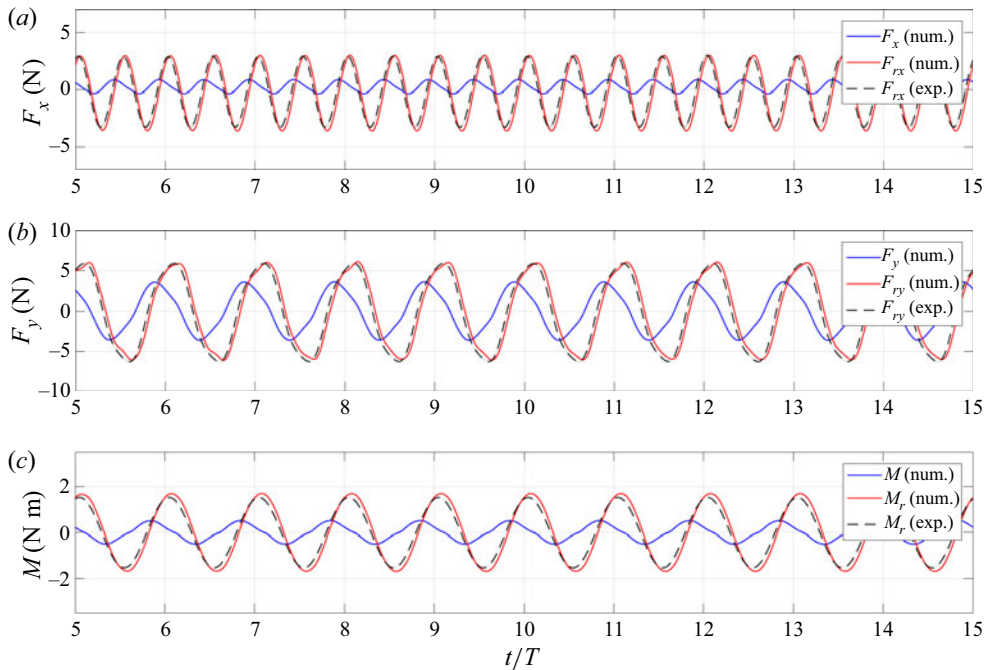


Figure 7. As in figure 6, but for  $\alpha_0 = 5^\circ$ ,  $U = 5 \text{ m s}^{-1}$  and  $f = 4 \text{ Hz}$  ( $Re = 9.57 \times 10^4$  and  $k = 0.752$ ).

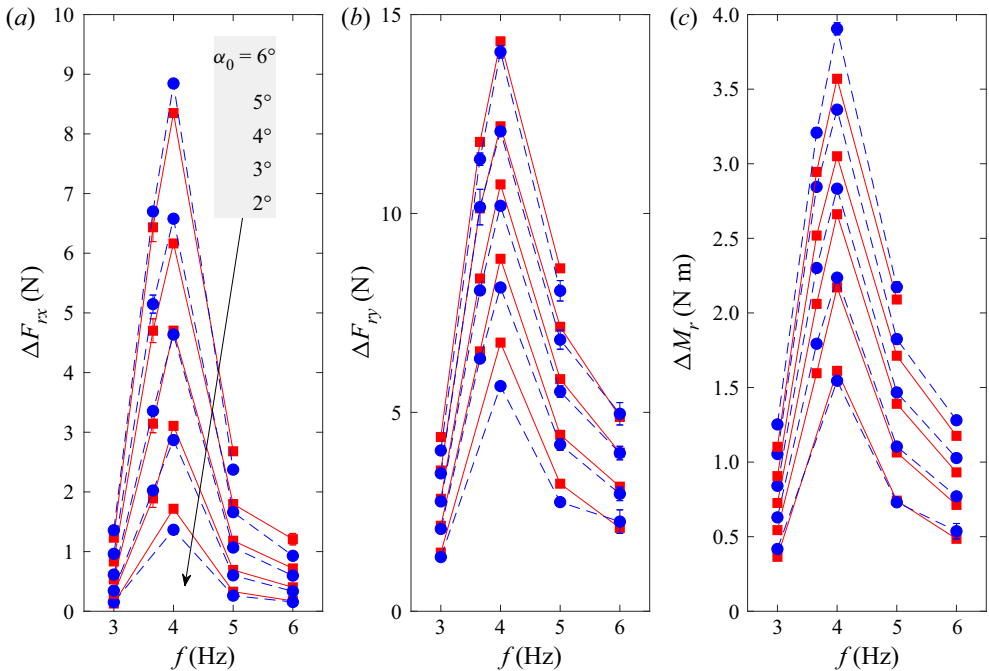


Figure 8. Comparison between the oscillation amplitudes of the two reaction force components,  $\Delta F_{rx}$  and  $\Delta F_{ry}$ , and the reaction moment,  $\Delta M_r$ , measured experimentally (red squares) and computed numerically (blue circles) for  $U \simeq 5 \text{ m s}^{-1}$  and different pitch amplitudes versus the frequency  $f$ . The different lines connecting the symbols (continuous for the experimental values and dashed for the numerical ones) correspond to, from bottom to top,  $\alpha_0 = 2^\circ, 3^\circ, 4^\circ, 5^\circ$  and  $6^\circ$ .

and for frequencies between 3 and 6 Hz. Notice that all the force and torque amplitudes show a pronounced peak at approximately  $f = 4 \text{ Hz}$ , roughly corresponding to the first resonance frequency of the present steel plate in an air current with velocity  $U = 5 \text{ m s}^{-1}$ :  $f_r \simeq 3.8 \text{ Hz}$  from linear potential flow theory (Fernandez-Feria & Alaminos-Quesada 2021), and  $f_{r0} \simeq 3.65 \text{ Hz}$  in vacuum, a frequency used in some of the plotted data. The largest discrepancies between measured and computed forces and moments occur near this resonant frequency for the largest pitch amplitude plotted,  $\alpha_0 = 6^\circ$ , especially for  $\Delta M_r$ , mostly due to limitations in the F/T sensor for these large torques and forces. For  $\alpha > 6^\circ$ , the measurements near the resonant frequency were out of the sensor range.

### 5. Conclusion

Novel relations have been derived between the instantaneous force and torque on a flexible pitching aerofoil as they are measured experimentally with standard F/T sensors with the force and moment that the fluid exerts on the aerofoil plus the aerofoil's inertia and structural tensions at the leading edge. The relations are validated by comparing high-resolution numerical simulations with direct force and torque measurements in a wind tunnel. Though in the present paper both fluid and reaction forces and torques have been computed numerically using the derived relations, and then compared with experimental measurements, the method may find a more useful application to derive the force and moment that the fluid exerts on the flexible pitching aerofoil from the direct force and torque measurements and subtracting the inertia force and torque and

## Force and torque reactions on a pitching flexible aerofoil

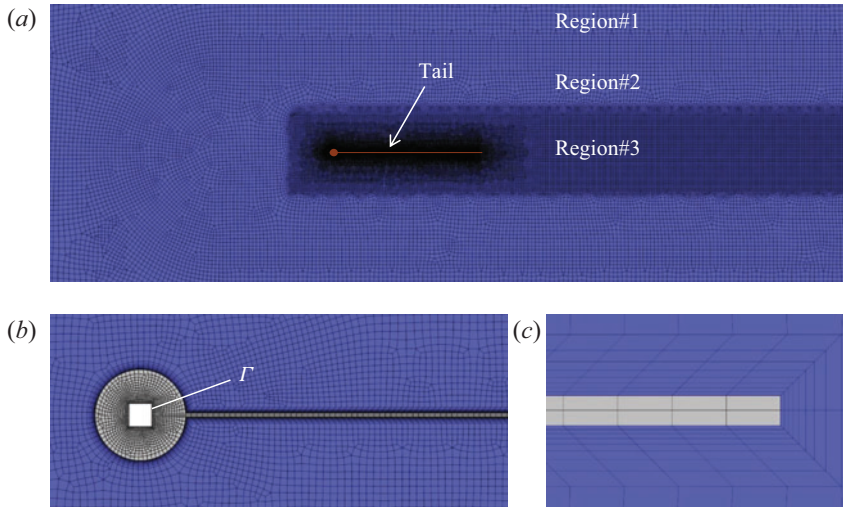


Figure 9. Three views of the mesh used in the computations (mesh #1). Here,  $\Gamma$  corresponds to the square boundary of the support.

structural tensions at the pivot axis from simultaneous video recording of the time evolution of a number of Lagrangian points along the aerofoil chord length. In fact, it is shown numerically that the technique captures accurately the contributions of the flexible aerofoil's inertia to the force and torque by taking into account just a few marker points along the chord length.

As a final remark, it is worth mentioning that the procedure described in § 2 may be extended easily to a flexible aerofoil undergoing general heaving and pitching motions about an arbitrary pivot axis, obviously adding new terms on the right-hand side of (2.8) and (2.9). But the most relevant inertial terms remain the same.

**Acknowledgements.** The computations were performed in the Picasso Supercomputer at the University of Málaga, a node of the Spanish Supercomputing Network.

**Funding.** This research has been supported by the Junta de Andalucía, Spain (UMA18-FEDER-JA-047 and P18-FR-1532).

**Declaration of interests.** The authors report no conflict of interest.

**Author ORCIDs.**

 R. Fernandez-Feria <https://orcid.org/0000-0001-9873-1933>.

### Appendix. Computational mesh details and mesh convergence study

Details of the mesh used in the computations are shown in figure 9. The boundary distance diffusion method is used to smooth the dynamic mesh, with diffusion parameter set to 1.75. The algebraic multi-grid with the conjugate gradient for pre-conditioning is used for stabilizing the dynamic mesh. As can be seen in figure 9(b), inside the head of the aerofoil, a square support with boundary  $\Gamma$  is included, necessary to impose the harmonic pitching motion.

To select the grid and time step, a grid convergence study was performed with three different meshes and time steps, doubling the number of cells and halving the time step. In particular: mesh #0 (coarse) with 51 465 cells, 283 cells along the profile and a time step

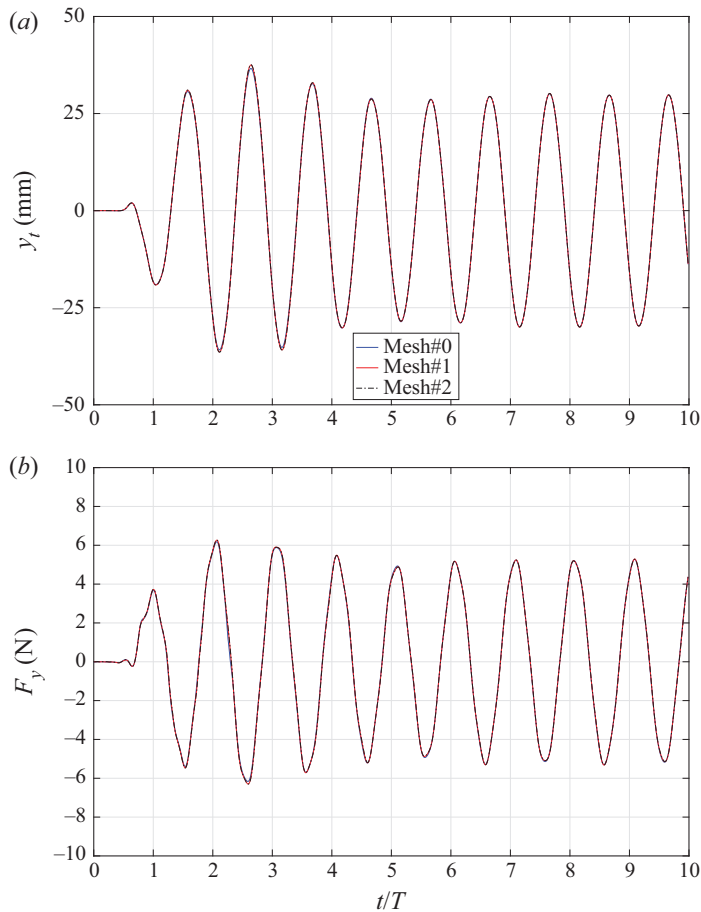


Figure 10. Mesh convergence study in terms of (a) the position of the trailing edge and (b) the lift force versus time. Here,  $U = 7 \text{ m s}^{-1}$ ,  $\alpha_0 = 3^\circ$  and  $f = 5 \text{ Hz}$ .

$\Delta t = 2 \times 10^{-4}$  seconds; mesh #1 (medium) with 99 298 cells, 400 cells along the profile and  $\Delta t = 10^{-4}$  seconds; mesh #2 (fine) with 190 914 cells, 566 cells along the profile and  $\Delta t = 0.5 \times 10^{-4}$  seconds. Two cells are placed in the thickness of the tail for the three meshes (see figure 9c). The time step was set to guarantee  $CFL < 5$  in all cases. The meshes of the fluid region include only quad elements with maximum skewness  $< 0.58$ . In order to capture correctly the boundary layer around the foil, we set an inflation layer of 8 cells with growth rate 1.2 and the first cell thickness of size 0.1, 0.071 and 0.05 mm for the meshes #0, #1 and #2, respectively (see figures 9b,c). This first layer thickness guarantees a maximum  $y^+ < 1$  on the foil wall, even for the case with the highest inlet velocity considered in this work.

The numerical results obtained with the three meshes for one of the most demanding cases (corresponding to  $Re = \rho Uc/\mu = 143\,760$ ) is shown in figure 10, indicating that the three meshes are very close to mesh independence. Thus all the results reported were performed with mesh #1. The results plotted in figure 10 are the position of the trailing edge  $y_t$  and the lift force  $L$  versus time.

REFERENCES

- ALBEN, S. 2008 Optimal flexibility of a flapping appendage in an inviscid fluid. *J. Fluid Mech.* **614**, 355–380.
- CONNELL, B.S.H. & YUE, D.K.P. 2007 Flapping dynamics of a flag in a uniform stream. *J. Fluid Mech.* **581**, 33–67.
- DEWEY, P.A., BOSCHITSCH, B.M., MOORED, K.W., STONE, H.A. & SMITS, A.J. 2013 Scaling laws for the thrust production of flexible pitching panels. *J. Fluid Mech.* **732**, 29–46.
- FERNANDEZ-FERIA, R. & ALAMINOS-QUESADA, J. 2021 Analytical results for the propulsion performance of a flexible foil with prescribed pitching and heaving motions and passive small deflection. *J. Fluid Mech.* **910**, A43.
- GHRALI, K. & JOHNSON, D.A. 2013 Dynamic stall simulation of a pitching airfoil under unsteady freestream velocity. *J. Fluids Struct.* **42**, 228–244.
- HEATHCOTE, S. & GURSUL, I. 2007 Flexible flapping airfoil propulsion at low Reynolds numbers. *AIAA J.* **45**, 1066–1079.
- KANG, C.K., AONO, H., CESNIK, C.E.S. & SHYY, W. 2011 Effects of flexibility on the aerodynamic performance of flapping wings. *J. Fluid Mech.* **689**, 32–74.
- KATZ, J. & WEIHS, D. 1978 Hydrodynamic propulsion by large amplitude oscillation of an aerofoil with chordwise flexibility. *J. Fluid Mech.* **88**, 485–497.
- LIGHTHILL, M.J. 1969 Hydromechanics of aquatic animal propulsion. *Annu. Rev. Fluid Mech.* **1**, 413–449.
- MACKOWSKI, A.W. & WILLIAMSON, C.H.K. 2015 Direct measurement of thrust and efficiency of an airfoil undergoing pure pitching. *J. Fluid Mech.* **765**, 524–543.
- MOORE, M.N.J. 2014 Analytical results on the role of flexibility in flapping propulsion. *J. Fluid Mech.* **757**, 599–612.
- PEDERZANI, J. & HAJ-HARIRI, H. 2006 Analysis of heaving flexible airfoils in viscous flow. *AIAA J.* **44**, 2773–2779.
- PENG, Z.R., SUN, Y., YANG, D., XIONG, Y., WANG, L. & WANG, L. 2022 Scaling laws for drag-to-thrust transition and propulsive performance in pitching flexible plates. *J. Fluid Mech.* **941**, R2.
- PLATZER, M., JONES, K., YOUNG, J. & LAI, J. 2008 Flapping wing aerodynamics: progress and challenges. *AIAA J.* **46**, 2136–2149.
- RAMANANARIVO, S., GODOY-DIANA, R. & THIRIA, B. 2011 Rather than resonance, flapping wings flyers may play on aerodynamics to improve performance. *Proc. Natl Acad. Sci. USA* **108**, 5964–5969.
- RIVAL, D.E. & VAN OUDHEUSDEN, B. 2017 Load-estimation techniques for unsteady incompressible flows. *Exp. Fluids* **58** (3), 20.
- SANMIGUEL-ROJAS, E. & FERNANDEZ-FERIA, R. 2021 Propulsion enhancement of flexible plunging foils: comparing linear theory predictions with high-fidelity CFD results. *Ocean Engng* **235**, 109331.
- SIALA, F.F., KAMRANI FARD, K. & LIBURDY, J.A. 2020 Experimental study of inertia-based passive flexibility of a heaving and pitching airfoil operating in the energy harvesting regime. *Phys. Fluids* **32** (1), 017101.
- SMITS, A.J. 2019 Undulatory and oscillatory swimming. *J. Fluid Mech.* **874**, P1.
- WU, T.Y. 1971 Hydromechanics of swimming propulsion. Part 1. Swimming of a two-dimensional flexible plate at variable forward speeds in an inviscid fluid. *J. Fluid Mech.* **46**, 337–355.
- WU, T.Y. 2011 Fish swimming and bird/insect flight. *Annu. Rev. Fluid Mech.* **43**, 25–58.
- WU, X., ZHANG, X., TIAN, X., LI, X. & LU, W. 2020 A review on fluid dynamics of flapping foils. *Ocean Engng* **195**, 106712.
- ZHU, Q. 2007 Numerical simulation of a flapping foil with chordwise or spanwise flexibility. *AIAA J.* **45**, 2448–2457.